

Full Length Article

Critical condition and transient evolution of methane detonation extinction by fine water droplet curtains

Jingtai Shi ^{a,b,c}, Yong Xu ^b, Wanxing Ren ^{a,c}, Huangwei Zhang ^{b,*}

^a School of Safety Engineering, China University of Mining and Technology, Xuzhou 221116, China

^b Department of Mechanical Engineering, National University of Singapore, 9 Engineering Drive 1, Singapore 117576, Republic of Singapore

^c Key Laboratory of Gas and Fire Control for Coal Mines, Xuzhou 221006, China



ARTICLE INFO

Keywords:

Methane detonation
Critical condition
Fine water droplet curtains
Mass loading
Droplet size
Eulerian–Lagrangian method

ABSTRACT

Two-dimensional numerical simulations with Eulerian–Lagrangian method and reduced chemical reaction model are conducted to study the methane detonation propagation across a water curtain with finite thickness. The critical length of the water curtain with sprayed droplets is determined through parametric simulations with different water mass loadings and droplet sizes. The influence of water curtain length on the methane detonation is examined by the trajectories of peak pressure and time history of average heat release rate. The results indicate that the water curtain not only inhibit the incident detonation wave, but also prevent the detonation re-ignition after the incident wave is quenched. Moreover, unsteady response of gaseous methane detonation to water curtain are analyzed. The detonation re-initiation process behind the water curtain near the critical loading is also captured. In addition, mechanism of detonation inhibition with fine water droplets are discussed. It is found that energy and momentum exchanges start immediately when the detonation wave enters the water curtain area, but the mass transfer starts well behind the detonation wave due to the finitely long droplet heating duration. It is shown that the convective heat transfer by water droplets plays a significant role in quenching a detonation.

1. Introduction

Methane explosions are common accidents in different applications, such as coal mines, metal mines, and natural gas pipelines. They may induce severe casualties and infrastructure damage. Zipf et al. [1] performed methane-air detonation experiments to characterize high pressure explosion processes that may occur in sealed areas of underground coal mines. The measured pressure behind the peak shock pressure ranged from 1.2 to 1.7 MPa, and agreed with computed Chapman–Jouguet pressure to within experimental error associated with this pressure measurement. Detonation cell patterns recorded with smoke foils showed irregular cell patterns for the methane-air test mixtures. Simulations were performed by Kessler et al. [2] to study the flame acceleration and deflagration-to-detonation transitions in large obstructed channels filled with a stoichiometric methane–air mixture using a single-step reaction mechanism. It is found that the detonations appear when shock reflections from channel walls and obstacles raise the local temperature in the unburned gases to the ignition point. Zhang et al. [3] obtained and analyzed the detonation velocity deficit and

cellular structure by a detailed investigation on the near detonation limits behavior of methane–oxygen mixtures in ducts. Wolański et al. [4] experimentally investigated propagation of detonation waves in methane-air mixtures. They found that the steady state wave propagation in a tube having a large length to diameter ratio, and the actual propagation velocities were close to the calculated Chapman–Jouguet velocities.

Effective suppression and mitigation technology are in high demand for methane explosion prevention and control [5]. Water spray mist is an ideal mitigant for gas explosion [6,7]. It can absorb considerable heat from gas phase due to large heat capacity and latent heat of evaporation and release water vapor to dilute flammable gas [8–10]. There have been studies about methane combustion or explosion suppression with water sprays. Qin et al. [11] pointed out that explosion overpressure magnitude and rise rate, as well as blast wave propagation velocity, decrease with the concentration of ultra-fine water mist based on their experiments in a transparent rectangular cavity. Jing et al. [12] found that ultra-fine water mist above a critical concentration (160 g/m³ – 800 g/m³) can eventually lead to detonation extinction. Moreover, the

* Corresponding author.

E-mail address: huangwei.zhang@nus.edu.sg (H. Zhang).

droplet size is also shown to have a significant influence on gas explosion suppression. van Wingerden et al. [13] experimentally studied the influence of droplet size on pressure development during gas explosions in congested areas. They found that the effective explosion-mitigating water-spray systems are those generating very small droplets (less than 10 μm), because droplets of these sizes can fully vaporize in the reaction zone. The influences of initial droplet size and spray concentration on methane explosion inhibition were also investigated numerically by Song and Zhang [14]. Their results show that the explosion gas temperature can be reduced by 52.2%, when the initial spray concentration is 1.5 kg/m^3 and the initial droplet size is 150 μm . Thomas et al. [15] demonstrated that water sprays can significantly reduce the pressure and impulse levels generated during flame acceleration.

Methane explosion properties are generally a deflagration process, but under certain conditions (gas concentration distribution conditions, detonation method and intensity, gas explosion space geometric characteristics, etc.), it may develop into a detonation. For example, confined space, such as coal mine tunnels, gas drainage pipelines, and natural gas pipelines, may cause gas detonation. Since detonation is a confluence of chemical reaction zone and leading shock [16], studies are also available to understand how the water droplets affect the reaction and/or shock fronts in detonations. Liang et al. [17] found that addition of ultrasonically generated water mist significantly prolongs induced explosion time due to the combined effects of physical suppression and chemical inhibition. Jarsale et al. [18] found that the presence of water sprays considerably affects the cellular structure, based on their detonation experiments with ethylene–air mixtures. However, the ratio of the hydrodynamic thickness over the cell size is not sensitive to the water loading. Chauvin et al. [19] found the peculiar pressure evolution after the transmitted shock wave in two-phase mixture and they also measured the overpressures under different water spray conditions. Simulations were performed by Ananth et al. [20] to examine the effects of mono-dispersed fine water mist on a confined blast. It is found that the latent heat absorption is dominant for blast mitigation, followed by convective heat transfer and momentum transfer. Schwer et al. [21] modeled the interaction between the water mists and flow field generated by an unconfined explosion. They found that the water mists mitigate the shock-front pressure through energy and momentum extraction from drag and vaporization. In addition, they also observed that droplet size and mass loading play a secondary role to the total amount of water between the observer and the explosive blast. Recently, Watanabe et al. [22] observed that the dispersed water droplets significantly alter the hydrogen detonation flow field, and water droplet evaporation mainly occurs around 10 mm behind the leading shock. They also found that the cellular patterns of detonation in dilute water sprays are more regular than those of droplet-free detonations [23]. Xu et al. [24] predicted the critical curves of hydrogen detonation extinction with fine water sprays and it is found that the critical mass loading of water sprays increases with the droplet size. They also discussed the evolution of the chemical structure in the induction zone during a detonation extinction process.

In these studies, the water mists are distributed as flooding species, i. e., in the entire domain. However, this is idealized, because in practical scenarios the water mists are from, e.g., ultrasonic mist generators. Because of the relatively long droplet dispersion timescale compared to the detonation propagation speed, uniform distribution of droplets is difficult to be realized. In this paper, the water curtain is considered, which is closer to the real situations. The critical parameters of the water curtain (including the length of the water curtain, droplet loading, and droplet diameter) will be explored. As far as we know, this has not been reported before in the literature. Two-dimensional simulations with Eulerian–Lagrangian approach will be carried out to study methane detonation propagation across a water spray curtain with finite thickness. A reduced chemical reaction model is used for methane combustion, and the evaporating water droplets are tracked individually by solving their velocity, temperature, and size. The critical conditions for

water mist to suppress methane detonation are explored, and the mechanism of methane detonation inhibition with water spray curtain is analyzed. The rest of the manuscript is structured as follows. The mathematical model is presented in Section 2, whilst the physical model is in Section 3. The simulation results and discussion will be given in Section 4, followed by the main conclusions summarized in Section 5.

2. Mathematical model

2.1. Gas phase

The governing equations of mass, momentum, energy, and species mass fraction are solved for compressible multi-component reacting flows. They respectively read

$$\frac{\partial \rho}{\partial t} + \nabla \cdot [\rho \mathbf{u}] = S_{\text{mass}}, \quad (1)$$

$$\frac{\partial (\rho \mathbf{u})}{\partial t} + \nabla \cdot [\mathbf{u}(\rho \mathbf{u})] + \nabla p + \nabla \cdot \mathbf{T} = S_{\text{mom}}, \quad (2)$$

$$\frac{\partial (\rho E)}{\partial t} + \nabla \cdot [\mathbf{u}(\rho E + p)] + \nabla \cdot [\mathbf{T} \cdot \mathbf{u}] + \nabla \cdot \mathbf{j} = \dot{\omega}_T + S_{\text{energy}}, \quad (3)$$

$$\frac{\partial (\rho Y_m)}{\partial t} + \nabla \cdot [\mathbf{u}(\rho Y_m)] + \nabla \cdot \mathbf{s}_m = \dot{\omega}_m + S_{\text{species},m}, \quad (m = 1, \dots, M-1). \quad (4)$$

In above equations, t is time and $\nabla \cdot (\cdot)$ is the divergence operator. ρ is the gas density, \mathbf{u} is the velocity vector, \mathbf{j} is the diffusive heat flux, and T is the gas temperature. p is the pressure, updated from the equation of state, i.e., $p = \rho RT$. R is the specific gas constant and is calculated from $R = R_u \sum_{m=1}^M Y_m W_m^{-1}$. W_m is the molar weight of m -th species and $R_u = 8.314 \text{ J}/(\text{mol} \cdot \text{K})$ is the universal gas constant. In Eq. (4), Y_m is the mass fraction of m -th species, and M is the total species number. $E \equiv e + |\mathbf{u}|^2/2$ is the total non-chemical energy, and e is the specific sensible internal energy.

The viscous stress tensor \mathbf{T} in Eq. (2) modelled by $\mathbf{T} = -2\mu[\mathbf{D} - \text{tr}(\mathbf{D})\mathbf{I}/3]$. Here μ is the dynamic viscosity and follows the Sutherland's law [25]. $\mathbf{D} \equiv [\nabla \mathbf{u} + (\nabla \mathbf{u})^T]/2$ is the deformation gradient tensor. In Eq. (4), $\mathbf{s}_m = -D_m \nabla (\rho Y_m)$ is the m -th species mass flux. The mass diffusivity D_m can be calculated through $D_m = k/\rho C_p$ with unity Lewis number assumption. C_p is the constant pressure heat capacity of the gas mixture. Moreover, $\dot{\omega}_m$ is the production or consumption rate of m -th species by all N reactions. In Eq. (3), the combustion heat release $\dot{\omega}_T$ is estimated as $\dot{\omega}_T = -\sum_{m=1}^M \dot{\omega}_m \Delta h_{f,m}^0$, in which $\Delta h_{f,m}^0$ is the formation enthalpy of m -th species.

2.2. Liquid phase

The Lagrangian method is used to model the dispersed liquid phase with a large number of spherical droplets [26]. The interactions between the droplets are neglected because we only study the dilute water sprays (initial droplet volume fraction being less than 0.1% [27]). Therefore, the governing equations of mass, momentum, and energy for individual water droplets read

$$\frac{dm_d}{dt} = -\dot{m}_d, \quad (5)$$

$$\frac{d\mathbf{u}_d}{dt} = \frac{\mathbf{F}_d + \mathbf{F}_p}{m_d}, \quad (6)$$

$$c_{p,d} \frac{dT_d}{dt} = \frac{\dot{Q}_c + \dot{Q}_{\text{lat}}}{m_d}, \quad (7)$$

where $m_d = \pi \rho_d d_d^3/6$ is the mass of a single droplet, and ρ_d and d_d are the droplet material density and diameter, respectively. \mathbf{u}_d is the droplet

velocity vector, \mathbf{F}_d and \mathbf{F}_p are the drag and pressure gradient force exerted on the droplet, respectively. $c_{p,d}$ is the droplet heat capacity at constant pressure, and T_d is the droplet temperature. In this work, both ρ_d and $c_{p,d}$ are dependent on the droplet temperature T_d [28].

The evaporation rate, \dot{m}_d , in Eq. (5) is modelled through

$$\dot{m}_d = k_c A_d W_d (c_s - c_g), \quad (8)$$

where A_d is the surface area of a single droplet, k_c is mass transfer coefficient, and W_d is the molecular weight of the vapor. c_s is the vapor mass concentration at the droplet surface, i.e.,

$$c_s = \frac{p_{sat}}{R_u T_f}, \quad (9)$$

where p_{sat} is the saturation pressure and is obtained under the assumption that the vapor pressure at the droplet surface is equal to that of the gas phase. The droplet surface temperature T_f is calculated from $T_f = (T + 2T_d)/3$ [29]. In Eq. (8), the vapor concentration in the bulk gas, c_g , is obtained from

$$c_g = \frac{p x_i}{R_u T_f}, \quad (10)$$

where x_i is the vapor mole fraction in the bulk gas.

The mass transfer coefficient, k_c , in Eq. (8) is calculated from the Sherwood number Sh [30]

$$Sh = \frac{k_c d_d}{D_f} = 2.0 + 0.6 Re_d^{1/2} Sc^{1/3}, \quad (11)$$

where D_f in Eq. (11) is the vapor mass diffusivity in the gas phase [31], and Sc is the Schmidt number of gas phase. The droplet Reynolds number in Eq. (11), Re_d , is defined as

$$Re_d \equiv \frac{\rho_d d_d |\mathbf{u}_d - \mathbf{u}|}{\mu}. \quad (12)$$

In Eq. (6), the Stokes drag \mathbf{F}_d is modelled as [32]

$$\mathbf{F}_d = \frac{18\mu}{\rho_d d_d^2} \frac{C_d Re_d}{24} m_d (\mathbf{u} - \mathbf{u}_d). \quad (13)$$

The drag coefficient in Eq. (13), C_d , is estimated as [32]

$$C_d = \begin{cases} 0.424, & \text{if } Re_d \geq 1000, \\ \frac{24}{Re_d} \left(1 + \frac{1}{6} Re_d^{2/3}\right), & \text{if } Re_d < 1000. \end{cases} \quad (14)$$

Since the ratio of gas density to the water droplet material density is well below one, the Basset force, history force and gravity force are not considered in Eq. (6) [27]. Besides, the pressure gradient force \mathbf{F}_p in Eq. (6) is from

$$\mathbf{F}_p = -V_d \nabla p \quad (15)$$

Here V_d is the volume of single water droplet.

The convective heat transfer rate \dot{Q}_c in Eq. (7) is calculated from

$$\dot{Q}_c = h_c A_d (T - T_d). \quad (16)$$

Here h_c is the convective heat transfer coefficient, estimated following Ranz and Marshall [30]

$$Nu = h_c \frac{d_d}{k} = 2.0 + 0.6 Re_d^{1/2} Pr^{1/3}, \quad (17)$$

where Nu and Pr are the Nusselt and Prandtl numbers of gas phase, respectively. In addition, \dot{Q}_{lat} in Eq. (7) is the heat transfer due to latent heat of droplet evaporation.

Two-way coupling between the gas and liquid phases is considered through Particle-source-in-cell approach [20]. The source terms, S_{mass} , S_{mom} , S_{energy} and $S_{species,m}$ in gas phase equations (1)–(4), are calculated

based on the droplets in the CFD cells

$$S_{mass} = \frac{1}{V_c} \sum_{i=1}^{N_d} \dot{m}_{d,i}, \quad (18)$$

$$S_{mom} = -\frac{1}{V_c} \sum_{i=1}^{N_d} \left(-\dot{m}_{d,i} \mathbf{u}_{d,i} + \mathbf{F}_{d,i} \right), \quad (19)$$

$$S_{energy} = -\frac{1}{V_c} \sum_{i=1}^{N_d} \left(-\dot{m}_{d,i} h_g + \dot{Q}_{c,i} \right), \quad (20)$$

$$S_{species,m} = \begin{cases} S_{mass} & \text{for } H_2O \text{ species} \\ 0 & \text{for other species.} \end{cases} \quad (21)$$

Here V_c is the CFD cell volume, N_d is the droplet number in one cell and h_g is the enthalpy of water vapor at droplet temperature. The droplet hydrodynamic force work is not included in Eq. (20), which is 2–3 orders of magnitude lower than the convective heat transfer and water vapor enthalpy in dilute spray detonations [24].

2.3. Computational method

The governing equations of gas and liquid phases are solved with *RyrhoCentralFoam* [33], which is developed based on the fully compressible non-reacting flow solver *rhoCentralFoam* in OpenFOAM 6.0 [34]. In this solver, the numerical method, sub-model and numerical implementations used have already been carefully validated and verified in previous work against experimental and theoretical data in our previous work [24,35–40].

Second-order backward method is employed for temporal discretization and the time step is about 1×10^{-10} s. The MUSCL-type Riemann-solver-free scheme by Kurganov et al [41]. with van Leer limiter is used for convective flux calculations in the momentum equations. Total variation diminishing scheme is applied for the convection terms in energy and species equations. Also, second-order central differencing scheme is applied for the diffusion terms in Eqs. (2)–(4). A reduced chemical reaction model (DRM 19) developed by Kazakov and Frenklach [42] is used for methane combustion, which contains 21 species and 84 reactions. Its accuracy in modelling detonation initiation and propagation has been systematically studied by Wang et al. [43], including the ignition delay time over a range of operating conditions. In the supplementary document, we also compare the C-J speed and pressure/temperature at the C-J and von Neumann locations of the ZND (Zeldovich, von Neumann, and Döring) structure predicted with DRM 19 and GRI 3.0 [44] and find that the results are close.

For the liquid phase, the water droplets are tracked based on their barycentric coordinates. The equations, i.e., Eqs. (5)–(7), are integrated by first-order implicit Euler method. Meanwhile, the gas properties at the droplet location (e.g., the gas velocity and temperature) are calculated based on linear weighted interpolation. The source terms, i.e., Eqs. (18)–(21), are calculated for the gas phase equations in a semi-implicit source approach. More detailed information about the numerical methods for gas and liquid phases can be found in Refs. [24,33].

3. Physical model and numerical implementation

Both two-dimensional and three-dimensional detonations are studied by different researchers [45–48], and it has been shown that they share some similarities in terms of detonation structure and some key characteristics. Therefore, 2D methane detonation propagation across a water spray curtain with a finite thickness is studied in this study and the schematic of physical model and computational domain is shown in Fig. 1. The length (x-direction) and width (y-direction) are 0.3 m and 0.025 m, respectively. It includes gaseous detonation development section (0 – 0.2 m) and two-phase section (0.2 – 0.3 m), as marked in Fig. 1. The whole domain is initially filled with stoichiometric $CH_4/O_2/N_2$ (mole ratio of 1:2:1.88) mixture. This composition is favorable for

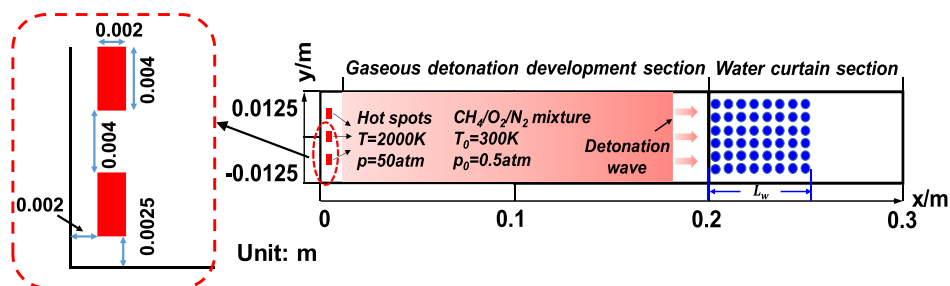


Fig. 1. Schematic of the computational domain. Blue dots: water curtain with the length of L_w . (For interpretation of the references to colour in this figure legend, the reader is referred to the web version of this article.)

detonation initiation and establishment of steadily propagation detonation wave within a short distance. The gas temperature and pressure are $T_0 = 300$ K and $P_0 = 50$ kPa, respectively. Based on the data provided by the GALCIT Explosion Dynamics Laboratory Detonation Database [49], it is seen that the greater the initial pressure, the smaller the cell width and hence induction length. Therefore, relatively low pressure (50 kPa) is conducive to predict the spray detonations with affordable computational cost.

In the two-phase section, ultrafine water droplets are loaded to mimic the water curtain implementation for practical detonation explosion prevention, as demonstrated in Fig. 1. In this work, the water curtain always starts at $x = 0.2$ and its streamwise length L_w is varied to study how it affects the effectiveness for detonation inhibition. Note in passing that if $L_w = 0.1$, then the water droplets exist in the whole two-phase section. It should be highlighted that the water droplets are always dispersed along the entire width as shown in Fig. 1.

Cartesian cells are used to discretize the domain in Fig. 1 and the mesh cell size transitions from $50 \mu\text{m}$ ($x = 0 - 0.14$ m) to $25 \mu\text{m}$ ($0.14 - 0.3$ m). To minimize the spatially variable resolution effects on detonation propagation, a refined area ($0.14 - 0.2$ m) with mesh size of $25 \mu\text{m}$ is included to connect the detonation development and two-phase sections. The resultant total cell numbers are 7,800,000. The Half-Reaction Length (HRL) estimated from the ZND detonation structure of the stoichiometric $\text{CH}_4/\text{O}_2/\text{N}_2$ mixture is about $2,200 \mu\text{m}$. Therefore, the resolution in the two-phase section is approximately 88 cells per HRL of C – J detonation. Considering the pronounced influence of the evaporating water droplets on the thermochemical composition in induction zone, actually over 88 cells can be expected within the HRL for spray detonations. Furthermore, a halved mesh resolution ($12.5 \mu\text{m}$) is also tested for the two-phase section. It is shown (from the supplementary material) that the detonation cell sizes are generally close to those with cell size of $25 \mu\text{m}$.

The detonation wave is initiated by three vertically placed hot spots ($2,000$ K and 50 atm) at the left end (see dimensions in Fig. 1). The three hot spots (size: $0.002\text{m} \times 0.004\text{m}$) are arranged vertically at equal intervals (see supplementary material). For all the gas–liquid detonation modelling in this work, a consistent initial field with propagating detonation wave at about $x = 0.196$ m (i.e., slightly before the two-phase section) is used. The upper and lower boundaries of the computational domain in Fig. 1 are periodic. For the left boundary ($x = 0$), the wave transmissive condition in OpenFOAM is enforced for the pressure, whereas the zero-gradient condition for other quantities. Zero-gradient conditions are applied for the right boundary at $x = 0.3$ m.

Monodispersed spherical droplets are considered in the water curtain. The initial water mass loading $z = 0.1-1.0$ and droplet sizes of $d_d^0 = 2.5-10 \mu\text{m}$ will be studied. Here the mass loading z is calculated based on the water mass to the gas mass in the actual gas-droplet areas. In OpenFOAM [34], a small thickness (out-of-plane direction in Fig. 1) of the computational domain is needed for 2D simulations (but no numerical fluxes are calculated in this direction). This thickness is relevant when we estimate the domain volume for mass loading and two-phase coupling (i.e., Eqs. 18 – 21). Moreover, the initial temperature,

material density and isobaric heat capacity of the water droplets are 300 K, 997 kg/m^3 and $4,187 \text{ J/kg}\cdot\text{K}$, respectively. Besides, the water droplets are assumed to be initially stationary (i.e., $u_d = 0$), which is reasonable due to typically small terminal velocities of fine droplets [19,50].

To reduce the computational cost, virtual parcel concept is used, and one parcel represents many water droplets with identical properties (e.g., temperature, velocity and size) [27]. In this work, the initial number of water droplets within each parcel is assumed to be 10, i.e., $n_p^0 = 10$, following our previous studies [24]. The droplet resolution has been studied in a case with $n_p^0 = 1$, and it is shown that the differences of droplet mass, surface area and interphase coupling are negligible (see supplementary document). When the water droplet breakup occurs subject to strong aerodynamic force from the high-Ma flows, this number density per parcel, n_p , increases considerably, but the total number of parcel (hence number of the solved Lagrangian equations, i.e., Eqs. 5 – 7) does not change throughout the simulation. In this study, droplet breakup process is modelled with the compressible version of the Pilch and Erdman model [51,52], which accounts for a range of liquid aerodynamic breakup regimes depending on different Weber numbers.

In this work, each simulation case is run with 360 processors for parallel computations in ASPIRE 1 Cluster in National Supercomputing Center in Singapore. It includes Fujitsu PRIMERGY servers providing total compute capacity of up to 1 PFlops and 128 GB memory per node or 5.33 GB memory per core. One case takes 72 h to be completed. More than 80 cases are simulated, which consume more than 2 million CPU hours in total.

4. Results and discussion

4.1. Critical conditions for detonation extinction

The critical length of the water curtain with sprayed droplets (L_{wc}) is determined through parametric 2D simulations with different water mass loadings and droplet sizes. The results are shown in Figs. 2 and 3, as a function of water mass loading z and initial droplet size d_d , respectively. Here detonation extinction is identified from the gradually decaying Heat Release Rate (HRR) as shown later (e.g., Fig. 4) and numerical soot foils. The critical curve (i.e., the solid lines in Figs. 2 and 3) is determined based on the critical water curtain length demarcating the detonation extinction (open symbols in Fig. 2) and propagation (solid symbols) cases. In Figs. 2 and 3, methane detonations are always quenched by the water curtains above the critical water curtain length.

As demonstrated in Fig. 2, for a fixed droplet size, the critical water spray curtain length L_{wc} decreases monotonically with water mass loading. For instance, when $d_d^0 = 5 \mu\text{m}$, $L_{wc} \approx 0.023$ m with $z = 0.1$. Nonetheless, when z is increased to 1.0, it is reduced to only around 0.003 m. This trend is observed for all the three droplet diameters in Fig. 2. Nonetheless, the dependence of L_{wc} on water mass loading z becomes weaker, when the mass loading is large. It is found that for $d_d^0 = 2.5$ and $5 \mu\text{m}$, when the mass loading is higher than 0.8, the critical water curtain lengths respectively approach the limiting values of

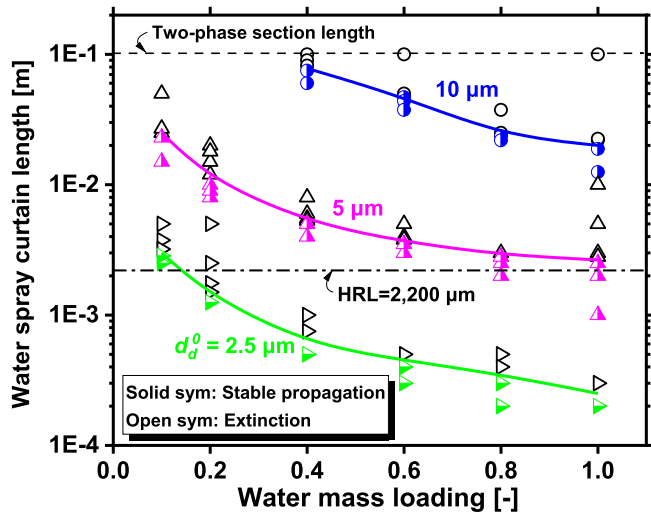


Fig. 2. Critical length of water curtain as a function of water mass loading. Open symbol: detonation extinction; solid symbol: detonation propagation. Circles: 10 μm ; upward triangles: 5 μm ; rightward triangles: 2.5 μm .

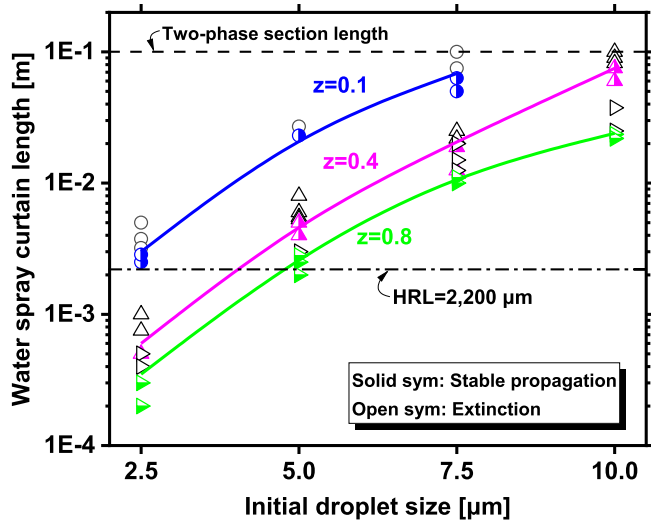


Fig. 3. Critical length of water curtain as a function of initial droplet size. Open symbol: detonation extinction; solid symbol: detonation propagation. Circles: $z = 0.1$; upward triangles: 0.4; rightward triangles: 0.8.

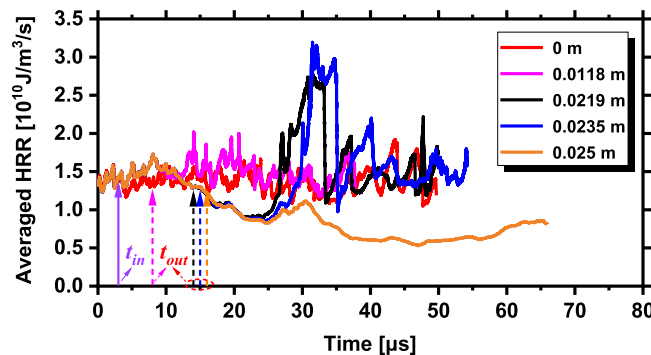


Fig. 4. Time history of average heat release rate with different water curtain lengths (L_w). $d_d^0 = 10 \mu\text{m}$ and $z = 0.8$. t_{in} and t_{out} : the instant when the detonation enters and leaves the water curtain.

0.0003 m and 0.002 m. This phenomenon may also exist for $d_d^0 = 10 \mu\text{m}$, although we do not simulate larger loadings (beyond 1.0) for it. This is a practically meaningful finding, because it implies that continuously increasing the water mass loading cannot ensure a smaller curtain length and meanwhile the effectiveness does not increase accordingly. Moreover, these limiting values of curtain lengths increases with the droplet sizes. This may be because they are associated with the characteristic timescales of the gas–liquid interactions, such as the thermal and momentum relaxation times [27].

In Fig. 3, for a fixed mass loading, the smaller the droplet size, the shorter the critical water curtain length. For instance, when the mass loading is 0.4, L_{wc} is 0.075 m for the initial droplet size of 10 μm , whereas it is reduced to 0.00063 m for 2.5 μm . This is caused by the fast evaporation and heating rate of the smaller droplets and hence higher effectiveness in detonation inhibition. Besides, the specific area of smaller droplets also increases under the same mass loading conditions. Therefore, they can absorb more heat from the gas phase, more appreciably reduce reaction rate (see supplementary document), and hence quench the detonation propagation. Also, due to the large amount of water vapor produced by droplets vaporization, the gas phase mixture would be diluted, leading to modulation of the local gas composition, thermodynamic conditions, and heat transfer properties. For practical explosion hazard prevention measures, the results in Fig. 3 indicate that with a well sprayed water curtain can considerably reduce the water curtain length. This is of utmost importance because it can minimize the detonation-affected areas, thereby reducing the casualties and infrastructure damage.

4.2. Unsteady response of gaseous methane detonation to water curtain

To demonstrate how the gaseous methane detonations are influenced by the different water curtain lengths, the unsteady detonation evolutions crossing the water curtain will be discussed in this section. Four typical cases with different water curtain lengths are selected for detailed analysis here, i.e., $L_w = 0.0118, 0.0219, 0.0235$ and 0.025 m. The unsteady phenomena observed therein are sufficiently representative among the simulation cases of this study. They have $d_d^0 = 10 \mu\text{m}$ and $z = 0.8$. The time evolutions of averaged HRRs are demonstrated in Fig. 4. Here the averaging is based on the domain of $x = 0.2 - 0.3$ m. Each curve corresponds to complete propagation of detonation wave or shock wave from $x = 0.2$ to 0.3 m, although the time durations in these cases are distinctive because of the different wave speeds. Note that the incident detonation wave arrives at the two-phase section at $t_{in} \approx 3 \mu\text{s}$ ($t = 0 \mu\text{s}$ corresponds to the initial field for spray detonation simulation in which the detonation lies at $x = 0.196$ m, as mentioned in Section 3). The result from $\text{CH}_4/\text{O}_2/\text{N}_2$ detonation without water curtain ($L_w = 0$ m) is also added in Fig. 4.

When $L_w = 0.0118$, the averaged HRR is generally steady but has some fluctuations. These fluctuations arise from the triple point collisions, which results in intermittently enhanced heat release. In this case, the evolution of HRR is close to that of the water-free case with $L_w = 0$ m. However, if L_w is further increased, e.g., 0.0219 and 0.0235 m, the averaged HRR gradually decreases when it travels in the water curtain. Note that the time when the detonation wave leaves the curtain is marked as t_{out} in Fig. 4. This signifies the gradually weakened detonative combustion in the gas phase by the water sprays. This tendency continues until 25 μs . After that, the averaged HRR suddenly increases and peaks around 35 μs , which is because detonation re-initiation occurs at the leeward side of the curtain (the unsteady process will be discussed at length later).

When the water curtain length is further increased to 0.025 m, as seen from Fig. 4, before 25 μs , the HRR evolves similar to those with $L_w = 0.0219$ and 0.0235 m. Nevertheless, no detonation re-initiation is observed in this case; instead, after 25 μs , the HRR gradually decreases, indicating the decoupling of the reaction front and leading shock front in

methane detonation. It should be mentioned that the finite HRR stems from the residual reaction front running in the shocked combustible mixtures. How the travelling reaction front evolves in a shocked combustible gas is also a great concern for mitigation of potential secondary explosion in real accidents, since they may develop into a new detonation through deflagration-to-detonation transition when some induction factor (such as obstacle, turbulence and shock focusing [53,54]) is present. Further studies on their longer evolutions after detonation extinction are merited as a future work.

Fig. 5 further demonstrates the numerical soot foils of the cases in Fig. 4. They are recorded from the trajectory of maximum pressure location, normally from the triple points, when the detonation wave propagates. The initial locations of the water curtains are marked with red boxes. The result from water-free detonation is added in Fig. 5(a) for comparison. It can be observed in Fig. 5 that presence of water curtain considerably changes the cellular structures of stoichiometric $\text{CH}_4/\text{O}_2/\text{N}_2$ detonations. Specifically, when $L_w = 0.0118$ m, the cell size within the water curtain is negligibly affected, through the comparisons between Fig. 5(a) and 5(b). However, beyond that, the cell size generally increases. For $L_w = 0.0219$ m and 0.0235 m in Fig. 5(c) and 5(d), the detonation waves propagate a distance in the water curtain, and the triple points are considerably reduced at around $x = 0.022$ m.

Afterwards, the peak pressure trajectories quickly fade, signifying the decoupling of leading shock front from the followed chemical reactions in the course of gaseous detonation extinction. However, at around $x = 0.024$ m, high-pressure spot arises in the middle of the domain width, resulting in X-shaped trajectories. This location is termed as Detonation Re-Initiation (DRI) point, marked in Fig. 5. Downstream of the DRI, transverse detonation can be observed (see the dark trajectories extending from DRI), which burn the mixture in the lengthened induction zone due to the detonation failure. Clear cellular structures appear again, but the morphology changes considerably compared to those before the detonation interacts with the water curtains. One peculiar phenomenon is appearance of many fine cells inside the primary cells. This is also observed by Gamezo et al. [55] in their studies about marginal detonation near the propagation limits. They attribute it to the secondary pulsations generated by unstable overdriven parts of the leading shock front. These changes include larger cell sizes and secondary peak pressure trajectory. This re-initiation phenomenon is consistent with the sudden increased HRR in Fig. 4.

When the water curtain length is increased to 0.025 m, one can see from Fig. 5(e) that the peak pressure intensity gradually becomes weak after crossing the water curtain. The pressure slightly increases at the original DRI point but is generally much lower than the counterpart in

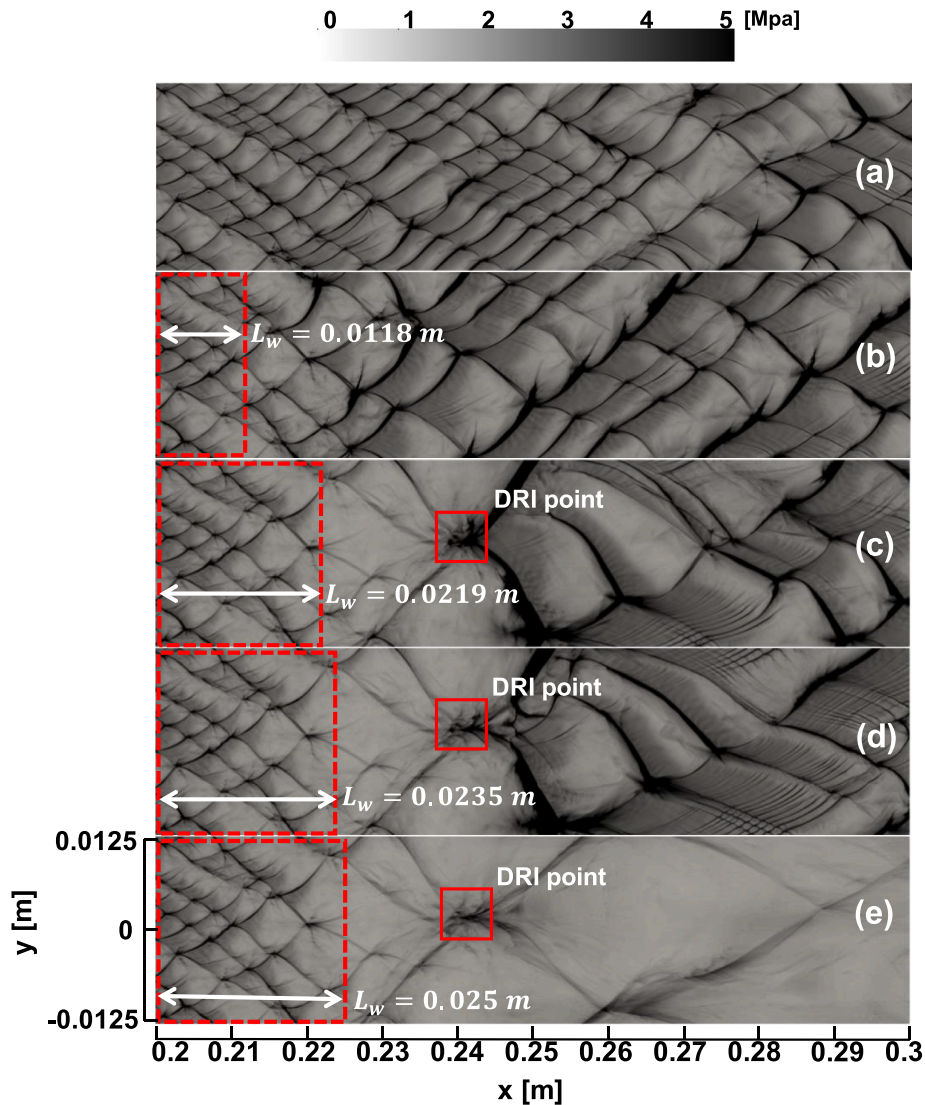


Fig. 5. Peak pressure trajectory of detonation wave affected by water spray curtains with the length of: (a) $L_w = 0$ m, (b) 0.0118 m, (c) 0.0219 m, (d) 0.0235 m, and (e) 0.025 m. $d_d^0 = 10 \mu\text{m}$ and $z = 0.8$. Dashed box: initial location of water curtain.

Fig. 5(c) and 5(d). In this case, no detonation development is observed downstream. This difference results from the increased length of the upstream water curtain. Here one can find that only slight increments of L_w leads to completely different outcomes of detonation evolutions. Therefore, caution needs to be exercised in practical water curtain implementations, because water curtain length close to the critical conditions is not recommended, although it may reduce the facility cost and complexity of the installation and arrangement. Based on Fig. 5, further increasing the water curtain length (>0.025 m) would always quench the incident methane detonation.

Fig. 6 shows the time evolutions of gas temperature in methane detonation without water curtain at six different instants, i.e., 12–32 μ s. It is seen that the detonation can propagate stably, with multiple Mach stems, incident waves and transverse waves. Stripe structures of gas temperature are observed behind the detonation front, due to the compression by the propagating transverse shock waves. Fig. 7 is the time sequence of gas temperature when the water curtain has a length of $L_w = 0.0118$ m, corresponding to Fig. 5(b). Nine instants are visualized after the detonation wave crosses the water curtain (its boundary is approximately sketched with the left and right contact surfaces in Fig. 7). At 12 μ s, the number of the Mach stem is appreciably reduced, leading to larger cell width, as seen from Fig. 5(b). The distance between the SF and RF is lengthened after the detonation wave crosses the water sprays. This can be clearly seen through comparing the results in Fig. 6 (a) and 7(a). Continued propagation of the methane detonation wave is observed until the end of the domain at 44 μ s, which is also manifested from the averaged HRR history in Fig. 4. Furthermore, the originally static water curtain (enclosed with the black lines) also moves along with the local high-speed flow field generated by the detonation wave, but the moving speed is obviously lower than the leading shock wave, due to the velocity relaxation time of the water droplets. Therefore, its direct inhibition influences on the travelling detonation wave quickly becomes weak, although it can still significantly lower the local gas temperature in the detonated areas.

Fig. 8 shows the counterpart results with a longer water curtain compared to that in Fig. 7, i.e., $L_w = 0.0235$ m. The contours of density and pressure are shown in the supplementary document. Due to larger L_w , the residence time of the methane detonation wave inside the water curtain increases. For instance, at 12 μ s, the detonation is still interacting with the dispersed fine water droplets. More pronounced effects on the detonation can be observed after the detonation crosses the curtain, such as at 16 and 20 μ s. The induction zone between SF and RF is thickened, based on Figs. 6 and 7. Moreover, in the middle of the leading SF, no following reaction fronts are presented immediately (e.g., at 20 and 24 μ s), indicating localized detonation extinctions. One can see from Fig. 8(e) to 8(f) that detonation re-initiation (see DRI point in Fig. 8e) occurs between 28 and 32 μ s, leading to an overdriven Mach stem in Fig. 8(f). For better interpretation of the re-initiation process, the evolutions of gas temperature, pressure and HRR at 29, 30 and 31 μ s are

shown in Fig. 9. One can see that at 29 μ s, the jet flows and triple points move towards each other. Their subsequent collision produces local high pressure and temperature. The gas in the induction area is ignited and two small forward hot jets are observed at 30 μ s, and the coupling between them and leading SF results in local detonative combustion. This further evolves into a larger Mach stem, as seen from the results at 31 μ s. Subsequently, from 36 μ s to 44 μ s, the detonation wave can continue propagating steadily, as found from Fig. 8(g)–8(i).

Plotted in Fig. 10 is the time sequence of the gas temperature at different time instants when the water curtain length is $L_w = 0.025$ m. Before 28 μ s, the evolutions of the detonation frontal structure are similar to the results in Fig. 8 with a shorter water curtain ($L_w = 0.0235$ m). A forward reactive jet is seen at 32 μ s in Fig. 10(f). Nonetheless, no mutual enhancement between the reactive jet and the leading curved SF is seen, and no detonative combustion develops. From 32 μ s to 44 μ s, although the reactive front grows considerably in the shocked $\text{CH}_4/\text{O}_2/\text{N}_2$ mixture, finite distance between the leading SF and RF always exists. Based on our numerical simulation results beyond 44 μ s, no detonation re-initiation happens and therefore the detonation is deemed fully quenched after it passes the water curtain with $L_w = 0.025$ m.

Fig. 11 shows the spatial evolution of the averaged leading shock propagation speed D in the foregoing two-phase methane detonations with different water curtain lengths. Note in passing that here the speeds are achieved with the segmented averaging method, to demonstrate the overall tendency of the detonation propagation behaviours, based on a timeseries (with a time interval of 1 μ s) of leading shock position. For comparisons, we also add the C-J speeds D_{CJ} of water-free $\text{CH}_4/\text{O}_2/\text{N}_2$ mixture for comparison, which is predicted by Shock and Detonation Toolbox [56] with the DRM 19 mechanism [42]. The detonation residence time in the curtain can be derived from t_{in} and t_{out} marked in Fig. 11.

As demonstrated in Fig. 11, the detonation propagation speeds of purely gaseous detonation are very close to the calculated C-J speed. However, the two-phase cases have speed deficits, relative to D_{CJ} . After the detonation wave passes the water curtain area, the speed of the detonation wave drops to the lowest value and then rises sharply near the DRI point. With increased L_w from 0.0118 m to 0.025 m, the detonation waves are gradually reduced, which is particularly true after the detonation wave leaves the water curtain. Specifically, for $L_w = 0.0118$ m, the speed fluctuates little near the C-J speed. For $L_w = 0.0219$ m and 0.0235 m, the detonation wave re-ignites after the water curtain, and the speed is higher than the C-J speed at some locations, probably caused by the overdrive effects. When $L_w = 0.025$, decoupling occurs after the detonation passes the water curtain. The wave speed decreases, well below the C-J value. Although the detonation wave is quenched, nonetheless, the blast wave degraded from the leading shock is still supersonic, with a speed of 1400–1600 m/s, which may still be disastrous for surrounding infrastructure and personnel. Therefore, how to quickly and effectively dampen the propagating blast wave necessitates further

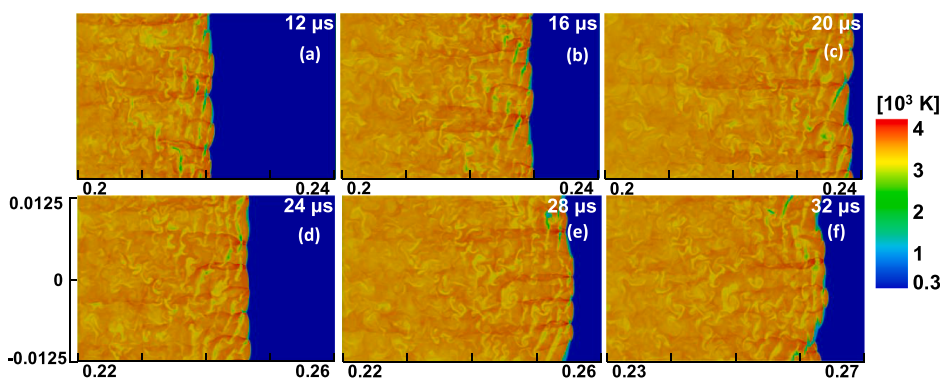


Fig. 6. Time sequence of gas temperature distributions in a droplet-free methane detonation. Axis label in m.

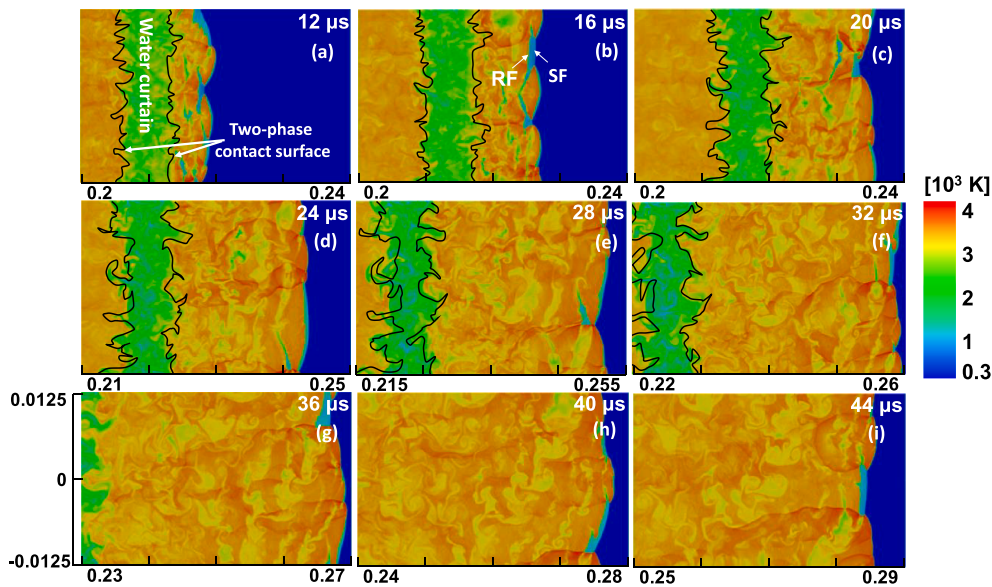


Fig. 7. Time sequence of gas temperature distributions in a spray detonation with water curtain length of $L_w = 0.0118 \text{ m}$. $d_d^0 = 10 \mu\text{m}$ and $z = 0.8$. Axis label in m. SF: shock front; RF: reaction front. Black lines: boundary of the water curtain.

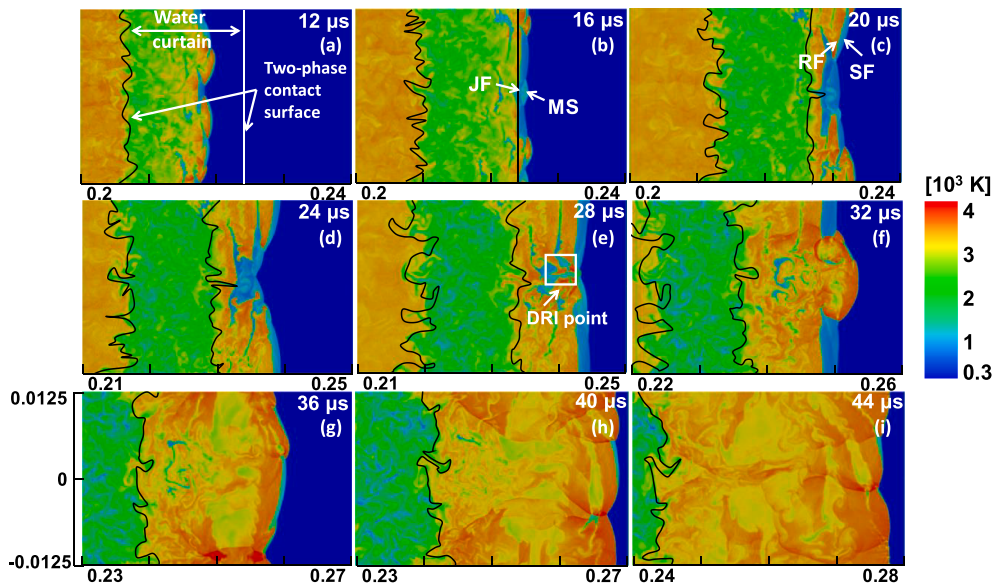


Fig. 8. Time sequence of gas temperature distributions in a spray detonation with water curtain length of $L_w = 0.0235 \text{ m}$. $d_d^0 = 10 \mu\text{m}$ and $z = 0.8$. Axis label in m. SF: shock front; RF: reaction front; MS: Mach stem; JF: jet flow. Black lines: boundary of the water curtain.

studies [21].

4.3. Mechanism of detonation inhibition with fine water droplets

The influences of water sprays on gaseous methane detonation are realized through mass, momentum, and energy exchanges between them. To reveal how these couplings play a role in quenching incident detonation, numerical experiments are performed. The base case is the extinction one with $L_w = 0.025 \text{ m}$ (termed as case e hereafter), and their information is listed in Table 1. In case e1, the droplet evaporation model is switched off to rule out the mass transfer (water vapour addition) effects. In case e2, the droplet evaporation and heat transfer are not considered. Therefore, in this case, there is no mass and heat transfer, but only momentum transfer between the gas and droplet phases.

Fig. 12 shows the trajectory of maximum pressures in cases e, e1 and e2. Note that the results for case e are identical to that in Fig. 5(e), where

the detonation wave is decoupled after crossing the water curtain with a weak DRI point at around $x = 0.24 \text{ m}$. For case e1, the detonation is also decoupled, but the re-initiation propensity is much lower, featured by weaker peak pressure values near the original DRI locus. One can see from case e2 that the detonation wave can propagate steadily after it passes the water curtain. The detonation cell size is increased to around 0.0125 m [the cell size λ is the apex-to-apex vertical (y -direction) distance] beyond the water curtain, indicating that the transverse waves are reduced and the detonation wave becomes more unstable. When the mass transfer and heat transfer models are de-activated in case e2, the propagation of detonation wave within the curtain is appreciably different from that in full case e. Moreover, the convective heat transfer has a more critical effect on detonation extinction, which can be found through the results in cases e1 and e2. From the three tests, we can have the following conjectures: (1) only momentum extraction by the gas phase (to accelerate the droplets) does not suffice to quench an incident

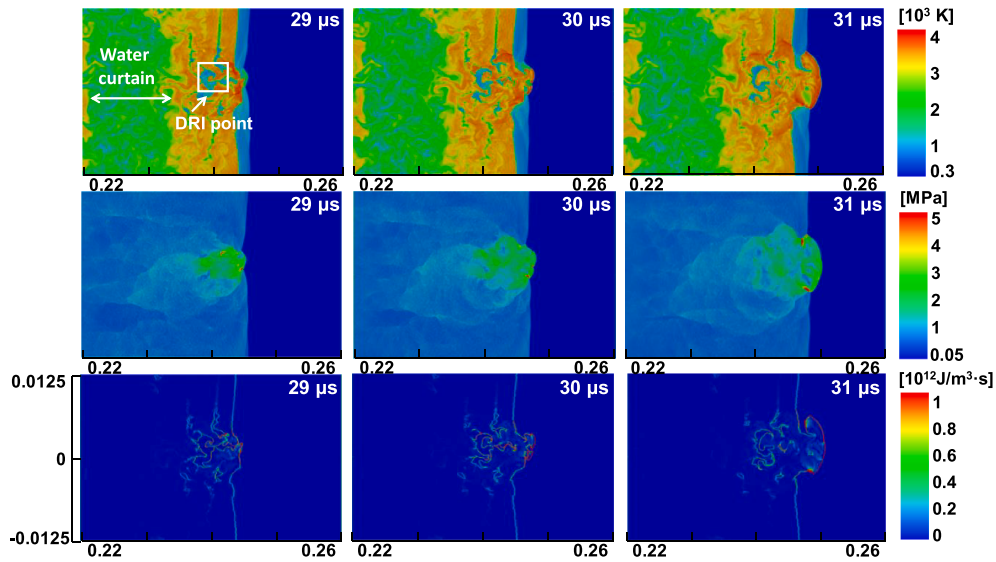


Fig. 9. Distributions of (first row) gas temperature, (middle row) pressure, and (bottom row) heat release rate when the detonation is re-initiated after the water spray curtain. $d_d^0 = 10 \mu\text{m}$, $z = 0.8$, and $L_w = 0.0235 \text{ m}$. Axis label in m.

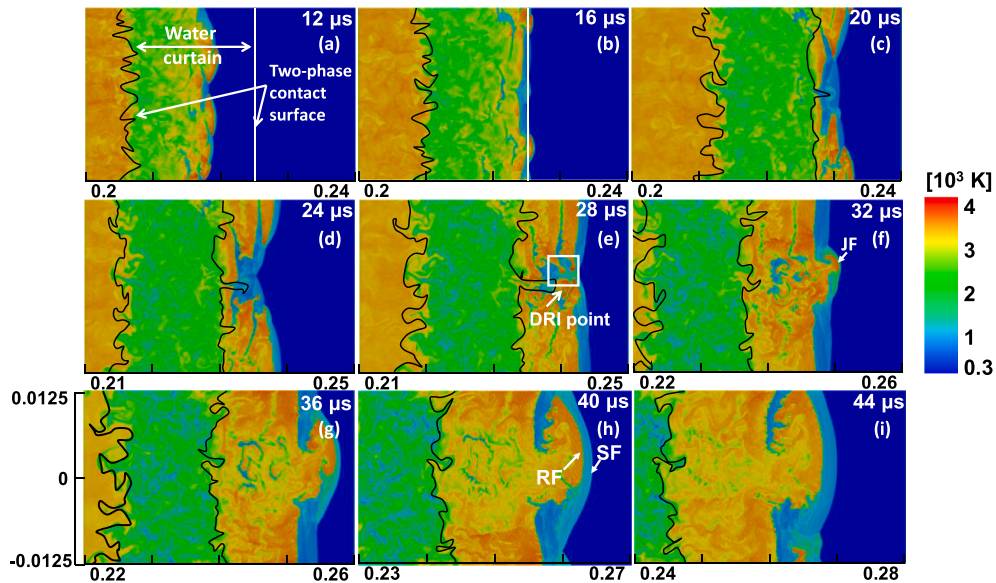


Fig. 10. Time sequence of gas temperature when the detonation is quenched after the water spray curtain. $d_d^0 = 10 \mu\text{m}$, $z = 0.8$ and $L_w = 0.025 \text{ m}$. Axis label in m.

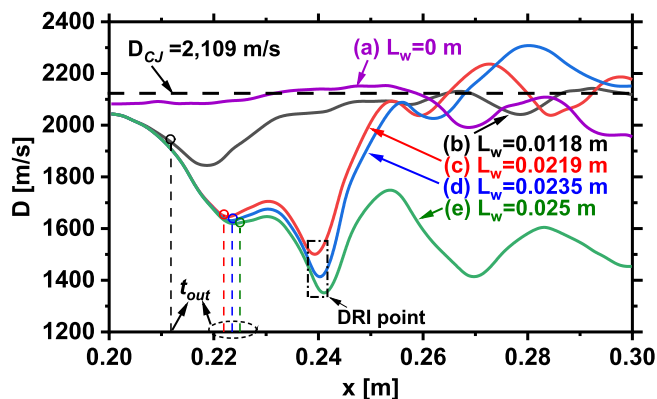


Fig. 11. Spatial evolution of averaged leading shock propagation speed. $d_d^0 = 10 \mu\text{m}$ and $z = 0.8$.

Table 1

Numerical experiments about detonation – droplet interactions.

Case	Droplet evaporation	Convective heat transfer	Momentum transfer	Average shock speed [m/s]	
				Water curtain	Whole domain (0.2 – 0.3 m)
e	✓	✓	✓	1,827	1,605
e1	×	✓	✓	1,841	1,472
e2	×	×	✓	1,960	2,027

detonation wave; (2) convective heat transfer is dominant in quenching a detonation wave; and (3) water vapour release from the droplets is shown to have limited influences on detonation inhibition. This is probably because the addition of water vapour can somehow facilitate

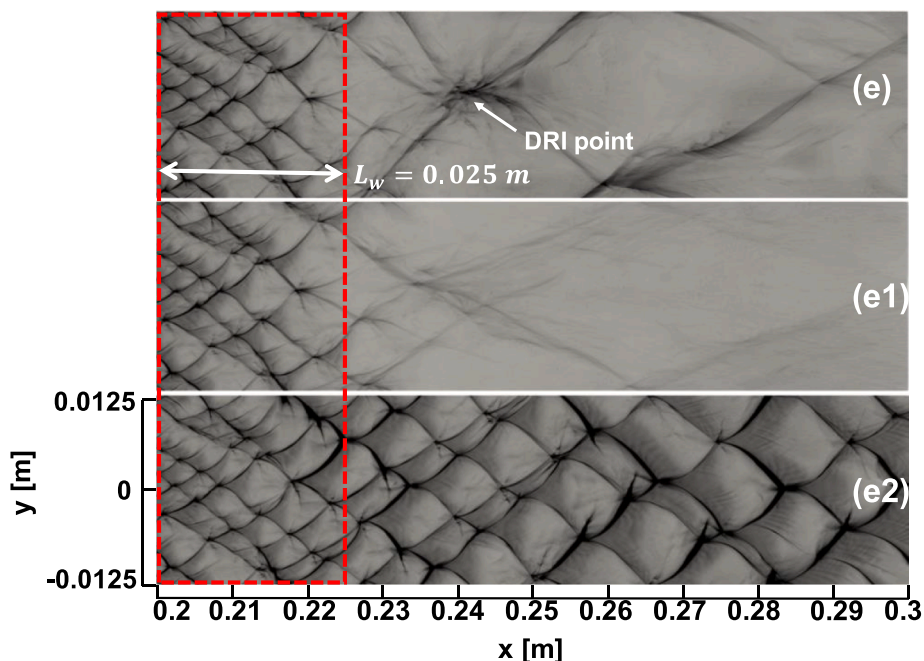


Fig. 12. Peak pressure trajectory of propagating detonation wave in cases e (top), e1 (middle) and e2 (bottom). Dashed box: initial location of water curtain.

the gas phase chemical reactions. However, the exact reason for the chemical reaction effects of water vapour from the droplet evaporation should be studied through examining how they affect methane explosion limits, which has been our on-going work. These conjectures will be further confirmed by the subsequent analysis in Figs. 15–18.

Fig. 13 further quantifies the evolutions of averaged shock propagation speed in cases e, e1 and e2. The calculation method is the same as for Fig. 11. In case e, the shock speed gradually decreases with some fluctuations when the detonation is decoupled after the water curtain. Compared with case e, the speed in case e1 is close to that of case e in the water curtain, and their average speed (crossing the detonation domain, i.e., 0.2–0.225 m) for crossing the detonation speeds are 1,827 and 1,841 m/s, respectively, as tabulated in Table 1. Beyond that, case e1 shows lower propagation speed compared to case e, corresponding to an average value (crossing the entire domain, i.e., 0.2–0.3 m, see Table 1) of 1,472 m/s. This indicates weaker shock intensity due to absence of re-initiation when the droplet evaporation is not considered in the numerical experiments. Both droplet evaporation and convective heat transfer are deactivated, stable detonation wave is observed in case e2. This corroborates the roles of interphase heat and mass exchanges in detonation inhibition, through comparisons of e2 and e. Based on our

results, the momentum exchange between gas and (non-evaporating / non-heated) droplets in e2 is generally higher than that in e1. For case e2, the shock is noticeably dampened in the water curtain, followed by a gradual increase to C-J speed after $x = 0.27$ m. This is reasonable because the detonation wave is travelling in the gas-only mixture at these locations. Compared to the other two cases, the speed of case e2 is generally higher when only the momentum exchange is considered.

In the rest of this section, we will analyze the droplet and gas phase properties in case e to further interpret the mass, momentum, and energy exchanges. Fig. 14 shows the time evolutions of water droplet temperature and diameter during the unsteady detonation extinction process. At $3 \mu\text{s}$, the detonation wave arrives at the water curtain (the initial distribution is $0.2 - 0.225$ m). In the shocked gas, the droplet temperature quickly rises, whilst the droplet size decays, due to aerodynamic fragmentation and evaporation. At $12 \mu\text{s}$, it takes about 3 mm for the droplets to get heated towards its saturated temperature. The water curtain behind SF moves following the local detonated flows, and the evaporating droplets exist for about 12 mm behind the leading SF. The droplet diameter is reduced to less than $3 \mu\text{m}$ for most of the shocked water curtain area. The smaller droplet size would lead to smaller thermal and momentum relaxation timescale and hence is more conducive for two-phase interactions in terms of mass, momentum, and energy [15].

Fig. 15 shows the profiles of water droplet temperature, velocity, and diameter at five instants from case e. Note that these quantities are obtained through arithmetic averaging of the corresponding Lagrangian quantities (i.e., the results in Fig. 14) along the y-direction. The overall evolutions of these quantities are consistent with the results in Fig. 14. As observed from Fig. 15(a), the droplet velocity gradually increases due to acceleration by the detonation wave, and the peak values are around 800 m/s. These peak values are reached after finite distance after leading SF. It can be seen from Fig. 15(b) that the droplet temperature rises more quickly. It takes about 3 mm to 4 mm to reach a saturation temperature of approximately 450 K. Aerodynamic fragmentation leads to quickly reduced droplet diameter as shown in Fig. 15(c), from the initial value ($10 \mu\text{m}$) to around $3-4 \mu\text{m}$. It can be seen from Fig. 15(c) that the droplets are gradually broken from $10 \mu\text{m}$ to about $3 \mu\text{m}$.

Fig. 16 shows spatial distributions of gas phase velocity and temperature at the same instants, which are obtained through density-

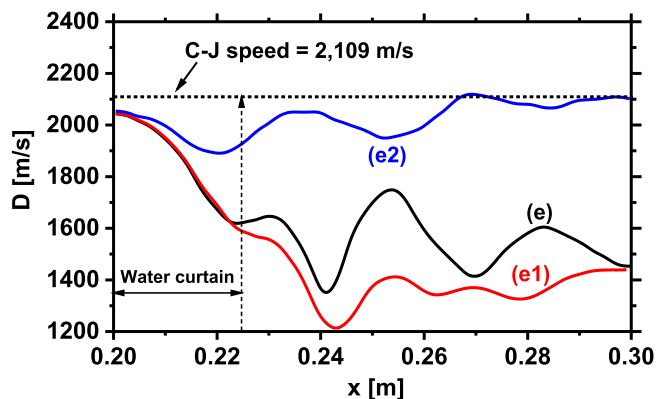


Fig. 13. Spatial evolution of averaged leading shock propagation speed in cases e, e1 and e2.

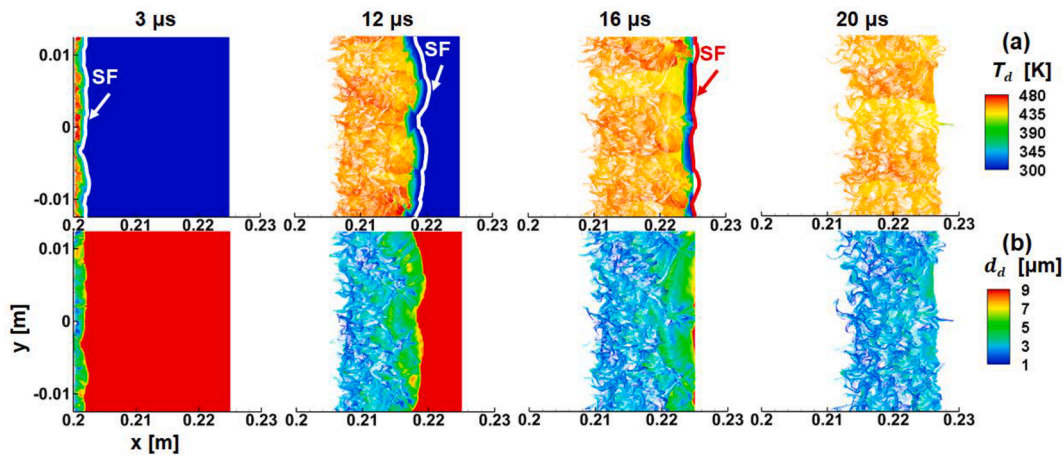


Fig. 14. Time evolutions of water droplets colored by: (a) droplet temperature and (b) droplet diameter. Results from case e.

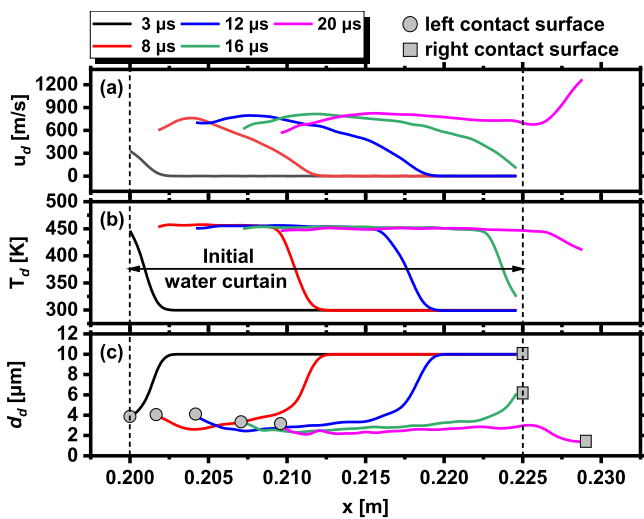


Fig. 15. Spatial distributions of (a) velocity (x -component), (b) temperature, and (c) diameter of water droplets at five instants in case e.

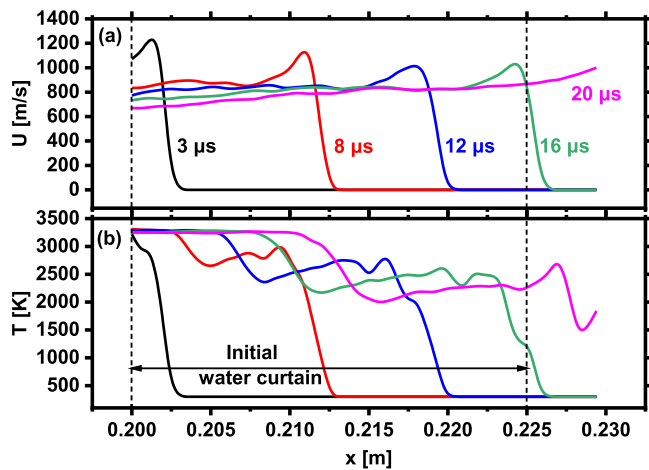


Fig. 16. Spatial distributions of gas (a) velocity and (b) temperature at five instants in case e.

weighted averaging along the y -direction. One can see from Fig. 16(a) that the averaged gas velocity grows quickly due to the arrival of the SF and decreases to about 800 m/s. As shown in Fig. 17(a), the gas and

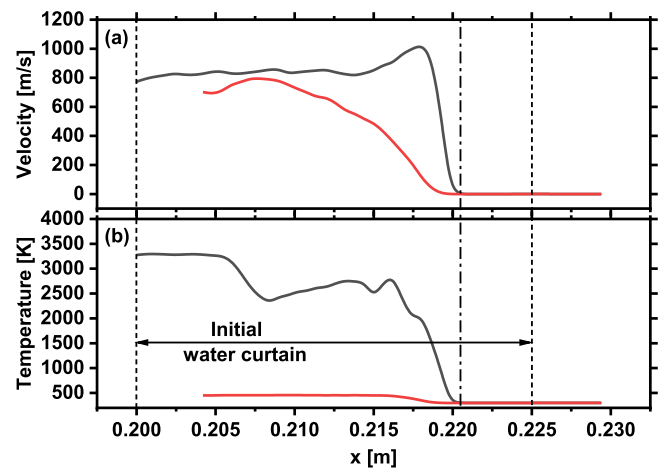


Fig. 17. Spatial distributions of (a) velocity and (b) temperature at 12 μ s in case e. Black lines: gas phase; red lines: liquid phase; dash-dotted lines: leading shock front. (For interpretation of the references to colour in this figure legend, the reader is referred to the web version of this article.)

droplet velocities are close at around $x = 0.2075$ m, where the droplet one peaks. This indicates a kinematic quasi-equilibrium location for gas and liquid phase. Nonetheless, further downstream, small velocity difference always exists. Meanwhile, it can be seen from Fig. 16(b) that the gas temperature also rises rapidly due to detonative combustion heat release, then have some finite variations between 2,000 K and 3,000 K, which spatially correspond to the droplet evaporation area. This can be clearly seen from Fig. 17(b). Considerable temperature difference exists in this area and therefore strong convective heat transfer for phase change would occur. Beyond the left contact surface, the gas temperature rises to a constant value of around 3300 K.

The transfer rates of mass, momentum, and energy between the gas and liquid phases are presented in Fig. 18. The results are calculated from the density-weighted average interphase transfer rates (S_{mass} , S_{mom} and S_{energy} in Eqs. 18–20). A positive mass (energy and momentum) transfer rate indicates that the corresponding transfer is from liquid (gas) phase to gas (liquid) phase. The results in Fig. 18 correspond to the same instants in Figs. 15 and 16. It can be seen from Fig. 18(b) and 18(c) that the transfer of heat and momentum from gas to liquid phases proceed immediately behind the leading shock (dash-dotted line). Their magnitude gradually increases towards the downstream and reach the peaks around 2 – 5 mm after the shock. The heat transfer rate is relatively distributed due to the interphase temperature difference as shown in Fig. 17(b). Conversely, the momentum transfer rates in Fig. 18(c) are

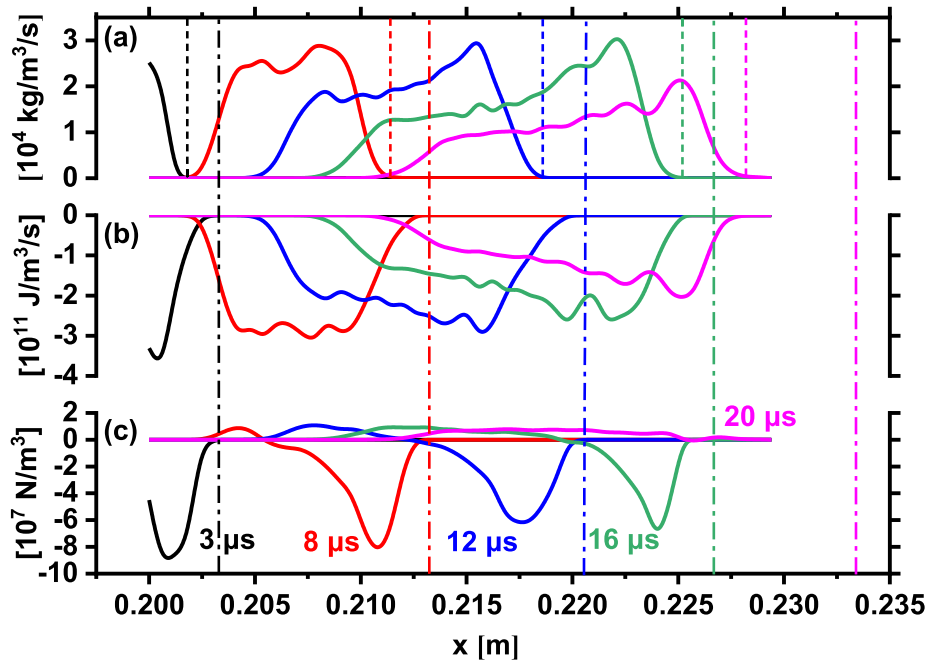


Fig. 18. Profiles of averaged transfer rates of (a) mass, (b) energy and (c) momentum at five instants. Dash-dotted lines: leading shock fronts; dashed lines: reaction fronts.

single-peaked. For instance, when $t = 12 \mu\text{s}$, the maximum is observed at around 0.2175 m, which corresponds to the maximum gas phase and relatively low droplet velocity, as can be found in Fig. 17(b). These tendencies about the energy and momentum exchanges can be found in all the shown instants.

However, the droplets start to vaporize around the RF due to increased temperature, and evaporation becomes significant well behind the detonation wave, i.e., the SF-RF complex (dashed lines in Fig. 18a). This is reasonable because of the finitely long droplet heating process, and implies that the water vapor from the water curtain may not have direct effects on the detonation structures, such as vapor dilution in the detonation induction zone. To reveal how the chemical effects of water vapour play a role in quenching incident detonations, numerical experiments have been performed (see supplementary document). It can be found that the role of water as third-body species has minor effects on the detonation wave behaviours. Besides, since the re-initiation point is

at the leeward of the water curtain (beyond the curtain), the foregoing effects of water vapor on detonation re-initiation are indirect and actually deemed an extended influence on the evolutions of the reaction front when the detonation wave crosses the water spray curtain. This also justifies the limited difference about detonation extinction between case e and case e1 in Fig. 12. Note that the droplet diameter is $10 \mu\text{m}$. For other cases with finer diameters (5 and $2.5 \mu\text{m}$), the same results are obtained.

Based on the preceding analysis, it is known that interphase heat transfer plays an important role in quenching a detonation with fine water sprays. Therefore, it would be helpful to compare the averaged power from the convective heat transfer and enthalpy of the added water vapor and the results are shown in Fig. 19. These two correspond to the mechanisms considered in the gas-liquid interaction, as shown in Eq. (20). The results are averaged from the Lagrangian droplet quantities along the y-direction. In general, for each instant, the power of

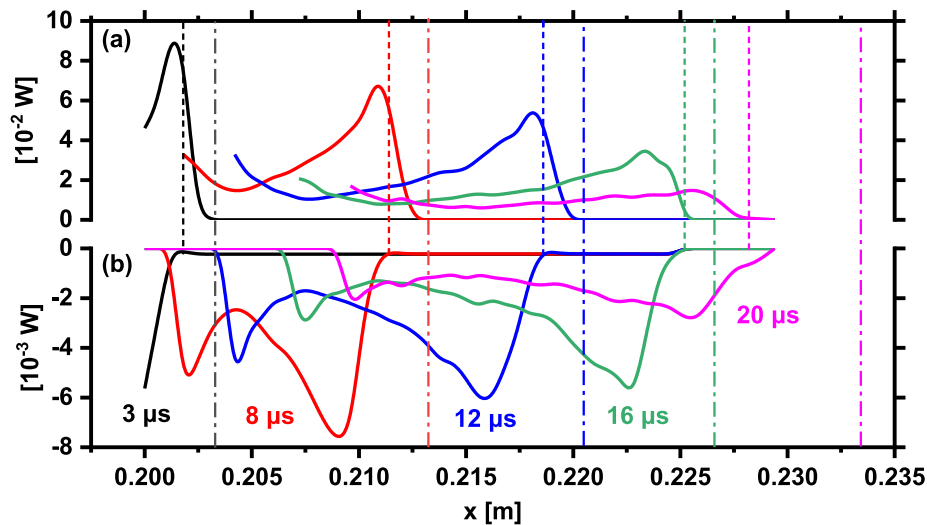


Fig. 19. Profiles of averaged power from (a) convective heat transfer and (b) water vapor enthalpy from the Lagrangian water droplets. Dash-dotted lines: location of the shock fronts, dash lines: location of reaction fronts.

convective heat transfer for the droplets is one order of magnitude higher than that for water vapor enthalpy. Since the droplet evaporation occurs well behind the RF and SF, the key mechanism for energy absorption near the detonation wave is convective heat transfer. This comparison further confirms conclusions from Figs. 12 and 13.

5. Conclusions

Extinction of methane detonation by fine water droplet curtains is studied with a hybrid Eulerian-Lagrangian method considering two-way gas – liquid coupling. Two-dimensional simulations with reduced chemistry reaction model for methane combustion are performed. Different water mass loadings and diameters in the curtain are taken into consideration.

The critical length of the water spray curtain is determined through parametric simulations. The results show that the critical curtain length decreases monotonically with water mass loading. For a fixed mass loading, the smaller the droplet size, the shorter the critical water curtain length. When the water mass loading is beyond 0.8, the critical length approaches a constant value, and these constant values increase with droplet diameter.

The influence of water curtain length on methane detonation is examined by the trajectories of peak pressure and time history of averaged combustion heat release rate. The results indicate that the water curtain length has significant effects on unsteady detonation propagation behaviors. For a length smaller than the critical value, the detonation can cross the water curtain, but becomes more unstable. When the length is close to the critical value, decoupling of SF and RF occurs and re-initiation occurs behind the water curtain. When the length is above the critical value, the incident detonation wave can be quenched without re-initiation.

Moreover, unsteady response of methane detonation to the water curtain is studied. General features of gas phase and liquid droplets and detailed detonation frontal structures are well captured. Incident detonations in different water curtain lengths are discussed, about the evolutions of frontal structure and detonation propagation speed. Compared to the gaseous cases, the two-phase cases have pronounced speed deficit, relative to the dry mixture C-J speed. It is seen that with increased curtain length from 0.0118 m to 0.025 m, the detonation wave speed generally decreases. When the water curtain is 0.025 m, although the detonation extinction occurs, nonetheless, the blast wave degraded from the leading shock is still supersonic.

In addition, mechanisms of detonation inhibition with fine water droplets are discussed. It is found that energy and momentum exchanges start immediately when the detonation wave enters the water curtain area, but the mass transfer starts well behind the detonation wave due to the finitely long droplet heating duration. It is shown that the convective heat transfer by droplet heating plays a significant role in quenching a detonation.

It should be mentioned that the stoichiometric $\text{CH}_4/\text{O}_2/\text{N}_2$ gas is used in this work and therefore the findings are specific to this mixture. When the $\text{CH}_4/\text{O}_2/\text{N}_2$ mixture is non-stoichiometric, the detonation wave may become more unstable with larger distance between transverse waves and hence larger cell sizes. Therefore, the detonation wave may demonstrate different behaviors in a gas-liquid two-phase environment. This is an interesting topic for our future work.

CRediT authorship contribution statement

Jingtai Shi: Conceptualization, Methodology, Formal analysis, Investigation, Writing – original draft. **Yong Xu:** Conceptualization, Methodology, Formal analysis, Software. **Wanxing Ren:** Supervision. **Huangwei Zhang:** Conceptualization, Methodology, Formal analysis, Writing – review & editing.

Declaration of Competing Interest

The authors declare that they have no known competing financial interests or personal relationships that could have appeared to influence the work reported in this paper.

Acknowledgements

This work used the computational resources of ASPIRE 1 Cluster in The National Supercomputing Centre, Singapore (<https://www.nsc.sg>), and Fugaku Cluster provided by RIKEN in Japan (<https://www.hpci-office.jp>) under the Fugaku Junior Researchers Project (Project ID: hp210196). HZ is supported by MOE Tier 1 grant (R-265-000-653-114). WR is supported by the Fundamental Research Funds for the Central Universities (2019XKQYMS75). JS is supported by the China Scholarship Council (202006420042).

References

- [1] Zipf RK, Gamezo VN, Sapko MJ, Marchewka WP, Mohamed KM, Oran ES, et al. Methane-air detonation experiments at NIOSH Lake Lynn Laboratory. *J Loss Prev Process Ind* 2013;26(2):295–301.
- [2] Kessler DA, Gamezo VN, Oran ES. Simulations of flame acceleration and deflagration-to-detonation transitions in methane-air systems. *Combust Flame* 2010;157(11):2063–77.
- [3] Zhang Bo, Shen X, Pang L, Gao Y. Methane-oxygen detonation characteristics near their propagation limits in ducts. *Fuel* 2016;177:1–7.
- [4] Wolański P, Kauffman CW, Sichel M, Nicholls JA. Detonation of methane-air mixtures. *Symp (Int) Combust* 1981;18(1):1651–60.
- [5] Yuan L, Smith AC. Numerical modeling of water spray suppression of conveyor belt fires in a large-scale tunnel. *Process Saf Environ Prot* 2015;95:93–101.
- [6] Catlin C. Passive explosion suppression by blast-induced atomisation from water containers. *J Hazard Mater* 2002;94(2):103–32.
- [7] Thomas GO. On the conditions required for explosion mitigation by water sprays. *Process Saf Environ Prot* 2000;78(5):339–54.
- [8] Ndubizu CC, Ananth R, Tatem PA, Motevalli V. On water mist fire suppression mechanisms in a gaseous diffusion flame. *Fire Saf J* 1998;31(3):253–76.
- [9] Grant G, Brenton J, Drysdale D. Fire suppression by water sprays. *Prog Energy Combust Sci* 2000;26(2):79–130.
- [10] Zhu D-M, Liang D, Liu J-Y. Numerical simulation of ultra-fine water mist extinguishing mechanism. *Procedia Eng* 2014;71:28–33.
- [11] Qin W, Wang X, Gu R, Xu H. Methane explosion overpressure and overpressure rise rate with suppression by ultra-fine water mist. *J Combust Sci Technol* 2012;18:90–5.
- [12] Jing Qi, Wang D, Liu Q, Chen Xu, Shen Y, Wang Z, et al. Inhibition effect and mechanism of ultra-fine water mist on CH_4/air detonation: Quantitative research based on CFD technology. *Process Saf Environ Prot* 2021;148:75–92.
- [13] van Wingerden K, Wilkins B, Bakken J, Pedersen G. The influence of water sprays on gas explosions. Part 2: mitigation. *J Loss Prev Process Ind* 1995;8(2):61–70.
- [14] Song Y, Zhang Qi. Quantitative research on gas explosion inhibition by water mist. *J Hazard Mater* 2019;363:16–25.
- [15] Thomas GO, Jones A, Edwards MJ. Influence of water sprays on explosion development in fuel-air mixtures. *Combust Sci Technol* 1991;80(1-3):47–61.
- [16] Lee JHS. The detonation phenomenon. 2008.
- [17] Liang Y, Zeng W. Numerical study of the effect of water addition on gas explosion. *J Hazard Mater* 2010;174(1-3):386–92.
- [18] Jarsalé G, Virot F, Chinnayya A. Ethylene-air detonation in water spray. *Shock Waves* 2016;26(5):561–72.
- [19] Chauvin A, Jourdan G, Daniel E, Houas L, Tosello R. Experimental investigation of the propagation of a planar shock wave through a two-phase gas-liquid medium. *Phys Fluids* 2011;23(11):113301. <https://doi.org/10.1063/1.3657083>.
- [20] Ananth R, Willauer HD, Farley JP, Williams FW. Effects of fine water mist on a confined blast. *Fire Technol* 2012;48(3):641–75.
- [21] Scherer DA, Kailasanath K. Numerical simulations of the mitigation of unconfined explosions using water-mist. *Proc Combust Inst* 2007;31(2):2361–9.
- [22] Watanabe H, Matsuo A, Matsuoka K, Kawasaki A, Kasahara J. Numerical investigation on propagation behavior of gaseous detonation in water spray. *Proc Combust Inst* 2019;37(3):3617–26.
- [23] Watanabe H, Matsuo A, Chinnayya A, Matsuoka K, Kawasaki A, Kasahara J. Numerical analysis of the mean structure of gaseous detonation with dilute water spray. *J Fluid Mech* 2020;887.
- [24] Xu Y, Zhao M, Zhang H. Extinction of incident hydrogen/air detonation in fine water sprays. *Phys Fluids* 2021;33(11):116109. <https://doi.org/10.1063/5.0071405>.
- [25] Ws LIL. The viscosity of gases and molecular force. *Lond Edinb Dublin Philos Mag J Sci* 1893;36:507–31.
- [26] Macpherson GB, Nordin N, Weller HG. Particle tracking in unstructured, arbitrary polyhedral meshes for use in CFD and molecular dynamics. *Commun Numer Methods Eng* 2009;25(3):263–73.
- [27] Crowe CT. Multiphase flows with droplets and particles. CRC Press; 2012.

- [28] Green DW, Southard MZ. Perry's chemical engineers' handbook. McGraw-Hill Education; 2019.
- [29] Sazhin SS. Advanced models of fuel droplet heating and evaporation. *Prog Energy Combust Sci* 2006;32(2):162–214.
- [30] Marshall WR, Ranz WE. Evaporation from drops—Part I. *Chem Eng Prog* 1952;48:141–6.
- [31] Fuller EN, Schettler PD, Giddings JC. New method for prediction of binary gas-phase diffusion coefficients. *Ind Eng Chem* 1966;58(5):18–27.
- [32] Liu AB, Mather D, Reitz RD. Modeling the effects of drop drag and breakup on fuel sprays. *SAE Trans* 1993;83–95.
- [33] Huang Z, Zhao M, Xu Y, Li G, Zhang H. Eulerian-Lagrangian modelling of detonative combustion in two-phase gas-droplet mixtures with OpenFOAM: validations and verifications. *Fuel* 2021;286:119402. <https://doi.org/10.1016/j.fuel.2020.119402>.
- [34] Weller HG, Tabor G, Jasak H, Fureby C. A tensorial approach to computational continuum mechanics using object-oriented techniques. *Comput Phys* 1998;12(6):620. <https://doi.org/10.1063/1.168744>.
- [35] Zhao M, Li J-M, Teo CJ, Khoo BC, Zhang H. Effects of variable total pressures on instability and extinction of rotating detonation combustion. *Flow, Turbul Combust* 2020;104(1):261–90.
- [36] Zhao M, Zhang H. Origin and chaotic propagation of multiple rotating detonation waves in hydrogen/air mixtures. *Fuel* 2020;275:117986. <https://doi.org/10.1016/j.fuel.2020.117986>.
- [37] Zhao M, Zhang H. Modelling rotating detonative combustion fueled by partially pre-vaporized n-heptane sprays. *ArXiv Prepr ArXiv200908617* 2020.
- [38] Zhao M, Zhang H. Large eddy simulation of non-reacting flow and mixing fields in a rotating detonation engine. *Fuel* 2020;280:118534. <https://doi.org/10.1016/j.fuel.2020.118534>.
- [39] Meng Q, Zhao M, Zheng H, Zhang H. Eulerian-Lagrangian modelling of rotating detonative combustion in partially pre-vaporized n-heptane sprays with hydrogen addition. *Fuel* 2021;290:119808.
- [40] Huang Z, Cleary MJ, Zhang H. Application of the sparse-Lagrangian multiple mapping conditioning approach to a model supersonic combustor. *Phys Fluids* 2020;32(10):105120. <https://doi.org/10.1063/5.0026654>.
- [41] Kurganov A, Noelle S, Petrova G. Semidiscrete central-upwind schemes for hyperbolic conservation laws and Hamilton-Jacobi equations. *SIAM J Sci Comput* 2001;23(3):707–40.
- [42] Kazakov A, Frenklach M. Reduced Reaction Sets based on GRI-Mech 2005;1(2):1–7.
- [43] Wang C, Qian C, Liu JianNan, Liberman MA. Influence of chemical kinetics on detonation initiating by temperature gradients in methane/air. *Combust Flame* 2018;197:400–15.
- [44] UC Berkeley Mechanical Engineering n.d. https://me.berkeley.edu/gri_mech/ (accessed November 24, 2021).
- [45] Dou H-S, Tsai HM, Khoo BC, Qiu J. Simulations of detonation wave propagation in rectangular ducts using a three-dimensional WENO scheme. *Combust Flame* 2008;154(4):644–59.
- [46] Cai X, Liang J, Deiterding R, Che Y, Lin Z. Adaptive mesh refinement based simulations of three-dimensional detonation combustion in supersonic combustible mixtures with a detailed reaction model. *Int J Hydrogen Energy* 2016;41(4):3222–39.
- [47] Tsuboi N, Katoh S, Hayashi AK. Three-dimensional numerical simulation for hydrogen/air detonation: Rectangular and diagonal structures. *Proc Combust Inst* 2002;29(2):2783–8.
- [48] Andrae S, Ballmann J, Müller S. Wave processes at interfaces. *Anal Numer Conserv Laws* 2005:1–25. https://doi.org/10.1007/3-540-27907-5_1.
- [49] Detonation Database – Cell length vs initial pressure; CH4-O2-Diluent n.d. https://shepherd.caltech.edu/detn_db/html/CH4-Ox5.html (accessed November 21, 2021).
- [50] Jourdan G, Biamino L, Mariani C, Blanchot C, Daniel E, Massoni J, et al. Attenuation of a shock wave passing through a cloud of water droplets. *Shock Waves* 2010;20(4):285–96.
- [51] Pilch M, Erdman CA. Use of breakup time data and velocity history data to predict the maximum size of stable fragments for acceleration-induced breakup of a liquid drop. *Int J Multiph Flow* 1987;13(6):741–57.
- [52] Lefebvre AH, McDonell VG. *Atomization and sprays*. CRC Press; 2017.
- [53] Dorofeev SB. Flame acceleration and explosion safety applications. *Proc Combust Inst* 2011;33(2):2161–75.
- [54] Oran ES, Gamezo VN. Origins of the deflagration-to-detonation transition in gas-phase combustion. *Combust Flame* 2007;148(1-2):4–47.
- [55] Gamezo VN, Vasil'ev AA, Khokhlov AM, Oran ES. Fine cellular structures produced by marginal detonations. *Proc Combust Inst* 2000;28(1):611–7.
- [56] Explosion Dynamics Laboratory n.d. <https://shepherd.caltech.edu/EDL/publicresources.html> (accessed October 12, 2021).